# Trismegisto – An Aortic Dissection Support Software with Automated Segmentation, SVM based Classification and OpenFOAM Flow Simulation

**Fernando José Domínguez-Morales** [1] **Enrique Emiliano Manjarrez-Peña** [1] **Brandon Orduña-Velazquez** [1] **Juan Pablo Rosado-Aíza** [1] **Nezih Nieto Gutiérrez** [1] **Valdo Jahuey-Moncada** [1] **Luis Alberto Muñoz Ubando** [1]

## Abstract

Aortic dissection (AD) is a critical cardiovascular emergency that conventionally relies on contrast-enhanced computed tomography for diagnosis, which poses limitations for contraindicated patients. To address this gap, Trismegisto is presented: a diagnostic support software that analyzes non-contrast enhanced CT (NCE-CT) scans by integrating automated segmentation, machine learning classification, and OpenFOAM-based flow simulation. The proposed methodology extracts geometric and morphological features from segmented, multicentric volumetric data, utilizing ANOVA and Kruskal-Wallis feature selection to train predictive algorithms. Evaluation of the models demonstrated that Support Vector Machine (SVM) and K-Nearest Neighbors (KNN) architectures achieved 98.3% validation accuracy, with the SVM model uniquely yielding zero false negatives. Ultimately, this work highlights the capability of machine learning to accurately identify pathological outliers from non-contrast imaging, providing a strong foundation for accessible diagnostic tools and hemodynamic visualization in global clinical settings.

## 1. Background

Aortic dissection (AD) represents a critical cardiovascular emergency, characterized by a tear in the intima of the aorta that allows both anterograde and retrograde blood flow into the tunica media, resulting in the formation of a false lumen (Umaña & Camacho, 2022). Clinically, AD is categorized using two main systems. The DeBakey classification is based on the origin and extent of the tear: type 1 originates in the ascending aorta and extends into the descending aorta through the aortic arch; type 2 is confined exclusively to the ascending aorta, while type 3 involves only the descending aorta. On the other hand, the Stanford classification simplifies this distinction: type A involves the ascending aorta with possible distal extension, while type B is characterized by not involving this region (Rodríguez et al., 2023).

In contrast-enhanced computed tomography studies, the false lumen is immediately identifiable due to the visualization of the flap or intima. Generally, the false lumen is larger due to its expansion and can compress the true lumen, which often acquires a crescent shape due to the differential pressure (Sica et al., 2025). The true lumen is distinguished by its continuity with major arterial branches, such as the renal or mesenteric arteries. Figure 1 presents a comparison of a type A AD computer tomography (CT), showing a contrast-enhanced acquisition (Image I) beside a non-contrast phase (Image J).

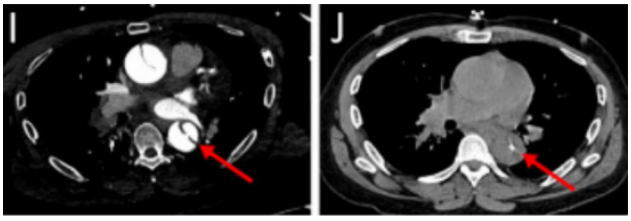



*Figure 1.* CT scans of type A AD with contrast (Image I) and type A AD without contrast (Image J) (Spangenberg et al., 2023).

To reduce mortality from the disease, the use of non-contrast enhanced computed tomography (NCE-CT) is desirable for the contraindicated population, although it traditionally lacks the desired specificity (Spangenberg et al., 2023). Subtle differences in grayscale tones are detectable by deep learning models, so that with a sample appropriate for the target demographic, tools can be created to significantly shorten diagnosis times (Hu et al., 2025).

Existing models for aortic dissection based on convolutional

[*]Equal contribution [1]School of Engineering and Science, Instituto Tecnológico y de Estudios Superiores de Monterrey, Monterrey, México. Correspondence to: <a00837476@tec.mx, a01369886@tec.mx, a01285759@tec.mx, a00835758@tec.mx, nezihniegu@tec.mx, a01571447@tec.mx, amunoz@tec.mx>.

*Proceedings of the $43^{rd}$ International Conference on Machine Learning*, Seoul, South Korea. PMLR 290, 2026. Copyright 2026 by the author(s).

neural network frameworks for semantic segmentation such as YOLO (Dong et al., 2024), nnU-net (Cheng, 2022) in combination with Pyradiomics, a radiomic features extraction library (Zhou et al., 2021; Van Griethuysen et al., 2017), achieve specificities of over 90%, although they are limited to a single country or region (Zhao et al., 2026).

## 2. Methodology

This work aims to document the development of a machine learning tool that analyzes NCE-CT scans to identify patterns associated with AD in a global population, with automated segmentation, classification and a semi-automated flow simulation module that allows for the visualization of hemodynamic behavior in the segmented aorta. The development and software pipeline is summarized in Figure 2.

### 2.1. Resources

The proposed environments were used for different stages in sample analysis. External tools such as MONAI (Cardoso et al., 2022), TotalSegmentator (Wasserthal et al., 2023), Pyradiomics (Van Griethuysen et al., 2017), OpenFOAM (Weller et al., 1998) and ParaView (Ahrens et al., 2005) are employed at different stages. The primary tools responsible for these distinct environments include Pyradiomics (which has no Python 3.10+ support, necessitating a Python 3.9 setup), PyTorch for feature extraction (which works best on modern Python 3.12 versions with CUDA integration), and OpenFOAM (a Linux-based pre-packaged environment utilizing WSL-Ubuntu). Additionally, a Python 3.11 MONAI environment was externally developed, since it will not be integrated into the final software. The comprehensive lists of specific packages, versions, and dependencies required for each of these four environments are detailed in the supplementary material.

### 2.2. Data Acquisition

The dataset used for the development was sourced from multicentric collaborators. Control patients were sourced from publicly available datasets from the Cancer Imaging Archive, as well as 3 subjects from the aforementioned collaborators; a total of 76 control subjects were pooled. The 13 pathologic patients were provided under ethical anonymity from the collaborators.

#### 2.2.1. Public Data

A composite of several public databases was selected, using the NLST (National Lung Screening Trial Research Team, 2013), LIDC-IDRI (Armato III et al., 2015), and RIDER Lung CT (Zhao et al., 2015) repositories. Sample selection was performed using a qualitative visual analysis, considering the quality of the NCE-CT scans and ensuring that, in the selected studies, the aortic morphology did not present any pathologies or abnormalities. This was done to maintain the "healthy" status of the patients, facilitating accurate segmentation and avoiding variability in both Hounsfield Units (HU) and aortic structure. The NLST repository includes over 26,000 patients from 33 specialized medical centers in the United States, whose images were acquired with a 2.5 mm slice thickness and low radiation dose—resulting in a lower signal-to-noise ratio—in subjects aged 55 to 74 years. The LIDC-IDRI repository comprises over 1,000 patients from various global institutions without specified geographic origin, with a demographic distribution of 53% men and 47% women, and a focus on lung cancer ranging from negative (healthy) cases to advanced stages. Although the repository contains slice thicknesses from 0.6 mm to 5.0 mm, for this study only those with a thickness $< 3.0$ mm and a pixel spacing between 0.5 mm and 0.8 mm were selected. Finally, the RIDER repository included data from 31 patients aged 60 to 70 years diagnosed with Non-Small Cell Lung Cancer (NSCLC); in this protocol, each patient underwent two CT scans with a 15-minute interval and slice thicknesses of 1.25 mm to 2.5 mm.

#### 2.2.2. Provided Data

The second part of the dataset consisted of NCE-CT scans, which were requested from a network of specialist physicians in a cardiology department. These studies corresponded to patients with clinical records of acute aortic syndrome. As part of the data collection protocol, the anonymization of patients' personal information and the use of a standardized nomenclature specifying the slice thickness and the manufacturer of the imaging equipment were required. From all the cases collected through this collaboration, 13 studies were selected that rigorously met the criteria for image quality, slice thickness, and consistency in the labeling of the records within the database.

#### 2.2.3. Data Augmentation

All data augmentation procedures were implemented in Python 3.11 using the MONAI framework. The original dataset consisted of 13 thoracic NCE-CT studies from patients with AD in DICOM format and the corresponding aortic segmentation masks in NIfTI format generated from the original imaging volumes. The extraction process for these masks is detailed in the following sections.

Prior to augmentation all datasets were standardized to a common spatial representation. CTs and masks were oriented to the RAS coordinate system and resampled to an isotropic voxel spacing of $1.5 \times 1.5 \times 1.5$ mm to ensure spatial consistency across the data acquired from different scanners and institutions.

To increase dataset variability and improve robustness, a 3D

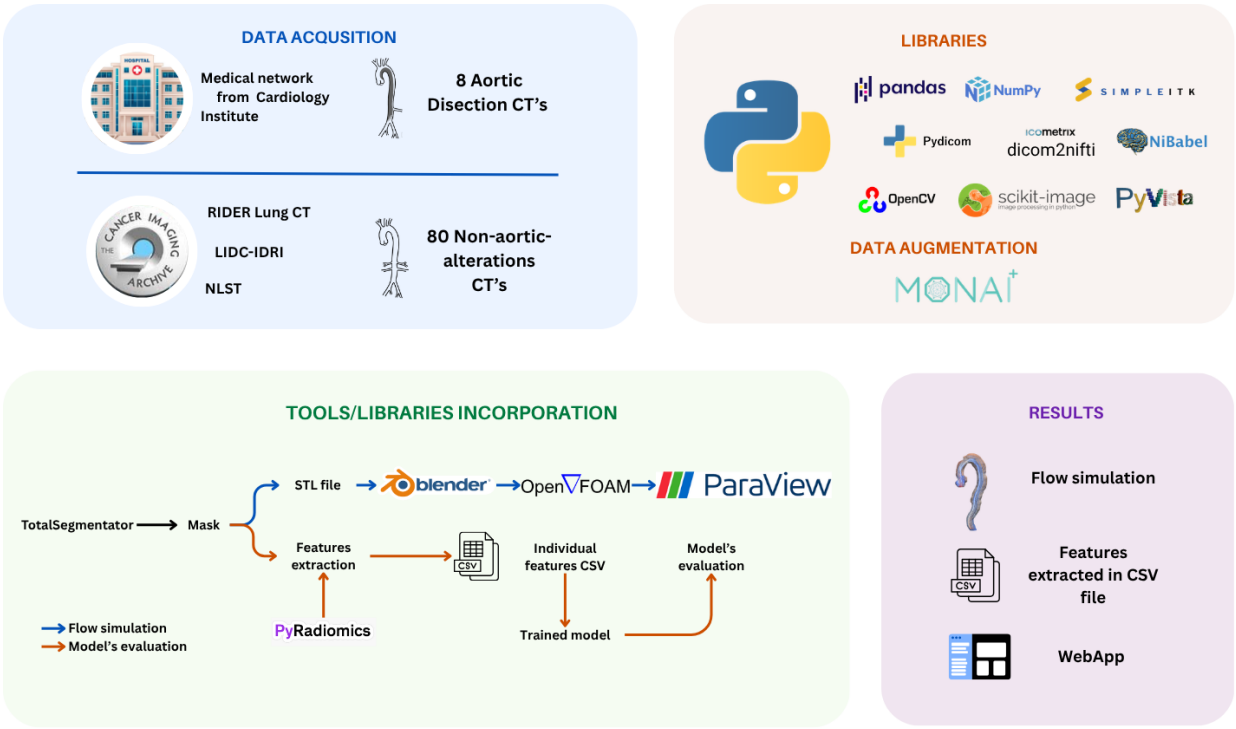



*Figure 2.* Summarized block diagram pipeline for sample analysis and flow simulation. Visual abstract of the Trismegisto framework.

volumetric data augmentation pipeline was implemented in which several spatial transformations were performed. The voxel-level intensity augmentation was performed through random HU perturbations with an offset range of $\pm 2$ HU applied directly to CT volumes. Spatial augmentation included independent random reflections along sagittal and coronal anatomical axes with a probability of 0.5 per axis, as well as affine geometric transformations applied with a probability of 0.7. Controlled rotational perturbations of up to $\pm 15^{\circ}$ around the three anatomical axes were introduced using a rotation range of 0.26 radians, while scaling transformations with a range of $\pm 15\%$ were applied to simulate moderate anatomical and acquisition variability while preserving clinically relevant morphology. All spatial augmentations were synchronously applied to both CT volumes and their corresponding segmentation masks to maintain voxel-wise anatomical alignment throughout the augmentation process.

Using the described augmentation pipeline, five synthetic volumetric variants were generated for each original patient study. Starting from an initial database of 13 pathological thoracic NCE-CT studies with their corresponding masks, the augmented dataset consisted of 65 volumetric pairs of CT and masks. The augmentation strategy was designed to increase anatomical and acquisition variability while preserving spatial consistency between imaging volumes and segmentation masks, thereby improving dataset diversity for downstream computational and machine learning applications. resulting in a volume of 78 samples in the pathologic group.

### 2.3. Preprocessing

All sourced studies were in DICOM format, which varies between different versions and software, but are readable with dicom2nifti. HU distributions ranged from $-3024$ to 15263 HU. No clipping was done, since feature extraction was focused on the ROI, with nothing from the rest of the image interfering. Slice thickness varied from 0.625 to 3 mm, and studies were taken with SIEMENS, TOSHIBA, GE or PHILIPS, without exclusion for manufacturer brand. All studies were converted to NIfTI using dicom2nifti, and reoriented to RPS (Right, Posterior, Superior as the positive direction) so that feature extraction works in all studies regardless of the original directionality.

### 2.4. Segmentation

Segmentation was performed using the TotalSegmentator tool, which has been trained on a wide range of CT and magnetic resonance imaging (MRI) scans. This software allows for the automated segmentation of various anatomical structures using specific commands, ranging from organs and teeth to complex systems integrating bone, vascular, mus-

*Table 1.* Inclusion and exclusion criteria for the pathological and control populations.

| Category | Criteria |
|---|---|
| Inclusion criteria | Patients diagnosed with AD, IMH, or PAU who underwent NCE-CT before intervention; patients aged 18 years or older. |
| Exclusion criteria | Patients with aortic endovascular treatment or stents; patients whose condition was caused by trauma; patients whose CT does not reach the thoracic cavity and aortic arch; patients with previous aortic surgery or modification; patients with heavy motion or otherwise unprocessable artifacts. |
| Control population criteria | CT scans should encompass the thoracic cavity whenever possible. The control population may include people with pathologies that do not impact the aorta's morphology or position. |
| Additional exclusion criteria for controls | Patients with AD, IMH, or PAU; patients whose aorta's position or morphology differs due to preexisting conditions. |

cle, and adipose tissue (Wasserthal et al., 2023) (Isensee, 2021). For this study, the process was specifically focused on delineating the aorta, processing the records in NIfTI (Neuroimaging Informatics Technology Initiative) format and using the segmentation label corresponding to this structure. Figure 3 illustrates an example of the dataset, showing the coronal, transverse, and sagittal planes, contrasting the original study with the resulting aortic segmentation mask.

### 2.5. Flow Simulation Module

The final software aims to automate the flow simulation entirely; however, for this work, 2 cases were simulated manually with the isolated Linux environment.

#### 2.5.1. STL Conditioning

A mask cleaning was performed; this process included isolating slices with content, removing the iliac arteries, and flattening the inlet and outlet surfaces, as well as eliminating artifacts. The dimensions were determined based on the voxel size obtained from the image metadata. Surface smoothing was applied to the resulting geometry. Additionally, the centroid coordinates within the mask were extracted, an essential element for running the simulation.

Two cases, one for each class, were processed to define

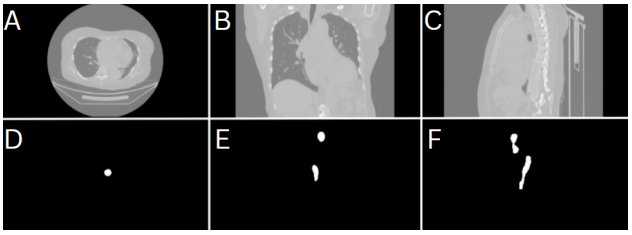



*Figure 3.* Multiplanar representation of a NCE-CT scan in a patient with AD and its respective segmentation mask. (A) Axial plane of the original study. (B) Coronal plane of the original study. (C) Sagittal plane of the original study. (D) Axial plane of the segmented aortic mask. (E) Coronal plane of the segmented aortic mask. (F) Sagittal plane of the segmented aortic mask.

the boundary conditions required for the numerical analysis. A scaling factor of $10^{-3}$ was applied to normalize the dimensions of the STL geometry and ensure accuracy in subsequent steps. Within the processing environment, the aortic body was segmented into its constitutive regions. The geometric positions and faces corresponding to the entry section, the exit section, and the peripheral aortic wall were identified and saved under the labels "Inlet", "Outlet", and "Wall", respectively. These designated sections and their respective names were stored as independent components within the STL file structure, establishing the definitive boundary conditions required to subsequently enter the fluid flow simulation system.

#### 2.5.2. Configuration

The hemodynamics within the pathological aortic geometries obtained with the masks were modeled using Computational Fluid Dynamics (CFD) to generate synthetic pressure and velocity fields which highly represented human conditions. All simulations were implemented using the OpenFOAM-11 (Weller et al., 1998) framework on a standardized Linux-based computational environment. The governing equations for the fluid domain were the transient, incompressible Navier-Stokes equations, solved using a Finite Volume Method (FVM) approach.

Anatomical segmentation masks were converted into computational domains through a multi-stage meshing pipeline. Initial STL geometries were encapsulated in a background hexahedral grid using `blockMesh`, with spatial resolution standardized via a localized bounding box maintaining a 20 mm safety margin to ensure the stability of the boundary level calculations. Volumetric discretization was executed via `snappyHexMesh`, applying a refinement at fluid-solid interfaces to capture complex aortic arch morphologies. A coordinate-based internal control point was defined as the luminal cell zone, followed by a snapping process to align

*Table 2.* Boundary Condition Specifications for Aortic Hemodynamics.

| PATCH | FIELD | CONDITION TYPE | PHYSIOLOGICAL VALUE |
|---|---|---|---|
| INLET | VELOCITY | FIXEDVALUE | 0.2 m/s |
| OUTLET | PRESSURE | FIXEDVALUE | 10.06 $m^2/s^2$ (80 MMHG) |
| WALL | VELOCITY | NOSLIP | IMPENETRABLE, ZERO-VELOCITY BOUNDARY |
| WALL | PRESSURE | ZEROGRADIENT | NORMAL PRESSURE EQUILIBRIUM |

the hexa-dominant cells with the surface curvature of the aortic wall. Finally, `createPatch` was utilized to redefine surface facets into functional patches for independent boundary condition assignment for the inlet, outlet and the wall of the model.

Blood was modeled as a Newtonian fluid, a standard assumption for larger vessels, with a constant density of 1060 $\mathrm{kg/m^3}$ and a kinematic viscosity of $1 \times 10^{-6}$ $\mathrm{m^2/s}$. Boundary conditions were assigned to simulate stable physiological states, as summarized in Table 2.

To maintain clinical relevance, the outlet pressure was fixed at a diastolic baseline of 80 mmHg. In OpenFOAM's incompressible solver, this was implemented as kinematic pressure, requiring a conversion factor of 133.32 $\mathrm{Pa/mmHg}$ to ensure numerical consistency with the physical properties of the blood.

Simulations were executed using the `icoFoam` solver, and numerical stability was strictly controlled by maintaining a maximum Courant Number ($Co$) of 0.8 through an adaptive time-stepping baseline of $\Delta t = 0.01$ s. Field data was extracted during the stable phase, 2 seconds after running the solver, employing a 200-point discretization along the entire aorta. The simulated velocity and pressure fields were exported into structured datasets.

## 2.6. Model Training

Unlike conventional models that use AD masks generated from contrast-enhanced studies for model training, this particular NCE-CT analysis—which lacks localization data—focused on evaluating changes in aortic morphology caused by the presence of dissection. These features are described below.

### 2.6.1. MASK FEATURES

From the preprocessed mask (see Section 2.5), geometric features related to the mask's volume (3D features) and individual slices (2D features) were extracted (see Figure 4). The 3D features include the total volume and surface area of the entire mask, as well as volumes by region, sectioned using a vertical cut through the middle of the mask and a horizontal cut at 55% of the height (see Figure 5) to obtain three regions: ascending arch, descending arch, and descent.

Meanwhile, the 2D features are extracted from the descent region for each slice, and representative statistics (maximum, minimum, mean, and standard deviation) are retained. These are calculated based on the major diameter, minor diameter, and eccentricity of the mask's centroid. Additionally, the area is included only for the slices corresponding to the aortic inlet and outlet.

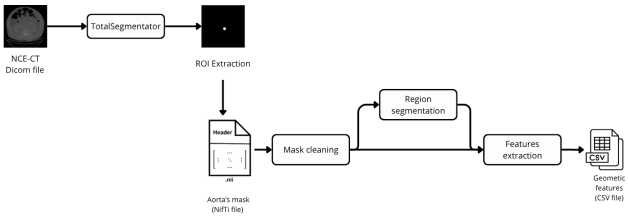



*Figure 4.* Pipeline for feature extraction from a NIfTI file.

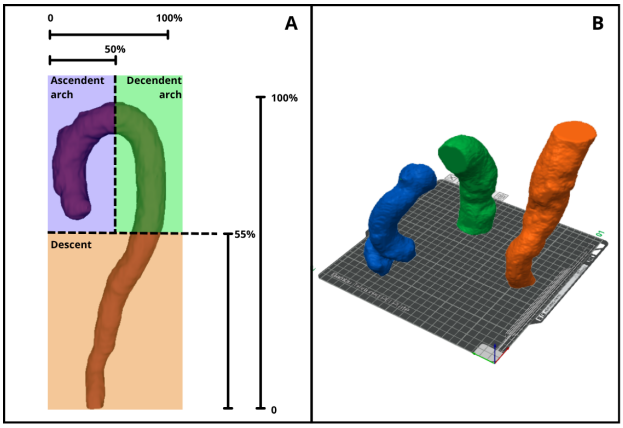



*Figure 5.* (A) Proportions employed for region segmentation. (B) Segmented parts (STL generated only for visual inspection).

### 2.6.2. RADIOMIC FEATURES

Pyradiomics is a Python library designed for easy use to obtain per-slice or per-volume radiomic features (Van Griethuysen et al., 2017). The full list of features can be found in the supplementary material. For the final software, the features provided by Pyradiomics will be evaluated using

importance scores against the mask features. For the current model, no radiomic features were used given that augmented data had sporadic HU variations (range defined previously). The tool, however, will be considered in future work.

#### 2.6.3. Feature Selection

Feature selection was performed utilizing both ANOVA and Kruskal-Wallis testing. To quantify the discriminative power of each feature, variables were ranked by their importance scores, which the software defines as the negative natural logarithm of the test's p-value ($-\ln(p)$). From the onset, descending arc volume, total surface area and total volume were excluded, given that the control population lacks a small part of the abdominal section of the aorta, so those values are biased. Statistical values like standard deviation of diameter are kept. All available models were trained with 5-fold cross-validation and tested 50 times with different random group-based splits: 3 pathological cases from the 13 were set apart, with their corresponding variations, totaling 18 pathological cases, as well as 18 control cases. The final split proportion is 23/77 after rounding. The aim is to maximize performance and minimize processing time for the aforementioned nature of diagnostic times, as well as maximize model interpretability to facilitate clinical interpretation of the result. The total features used were 12, with 4 extra features being removed on account of a low importance score on both tests (see Figure 6) ($< 3$; e.g. $p > 0.05$).

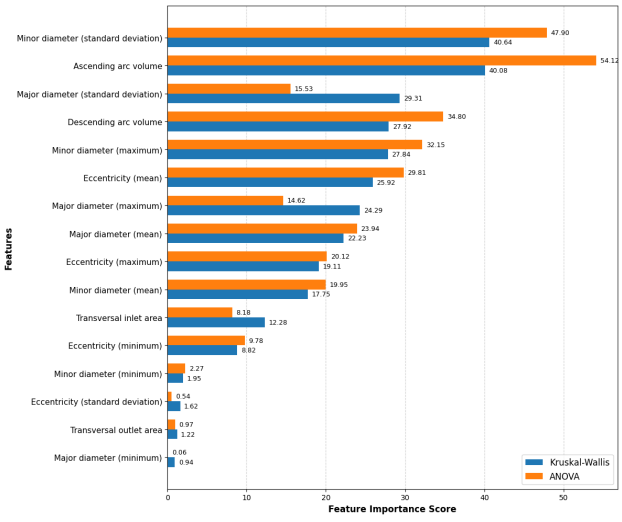



*Figure 6.* Feature importance scores.

## 3. Results

The experimental results are presented from two complementary perspectives. First, the classification performance of the machine-learning models is reported using validation and held-out test results, with emphasis on correctly identifying AD cases while minimizing false negatives. Second, the hemodynamic simulations are visualized to qualitatively and quantitatively compare healthy and pathological aortic flow patterns. Together, these results assess both the diagnostic performance of the predictive models and the physiological interpretability of the simulation-based analysis.

### 3.1. Model Results

The highest performing architectures were the Support Vector Machine (SVM) and K-Nearest Neighbors (KNN). Median performing iterations of the random data splits were chosen, in which both Linear SVM and Fine KNN achieved 98.3% accuracy on the validation set. Notably, the SVM model yielded zero false negatives on validation and testing, as shown in Table 3. Upon final evaluation, the SVM model achieved 97.2% accuracy on the held-out test set, with all 18 AD (aortic dissection) cases and 17 of 18 NC (normal control) cases correctly classified, as also shown in Table 3.

*Table 3.* Confusion matrices for the SVM model. The validation matrix shows the model selection performance, while the held-out test matrix shows the final evaluation with the separate testing set.

| Dataset | True Class | Predicted AD | Predicted NC |
|---|---|---|---|
| Validation | AD | 60 | 0 |
| | NC | 2 | 56 |
| Held-out test | AD | 18 | 0 |
| | NC | 1 | 17 |

Comparatively, the KNN model showed similar performance, as seen in Table 4.

*Table 4.* Confusion matrices for the KNN model.

| Dataset | True Class | Predicted AD | Predicted NC |
|---|---|---|---|
| Validation | AD | 59 | 1 |
| | NC | 1 | 57 |
| Held-out test | AD | 18 | 0 |
| | NC | 1 | 17 |

### 3.2. Flow Simulation Visualization

To better visualize the results obtained for the flow simulation, the ParaView 5.11.2 (Ahrens et al., 2005) software was implemented in the code in which the resulting graphs and images were displayed. Two major visualization strategies were implemented using this software:

(a) Flow patterns were visualized through volumetric rendering of the velocity magnitude and pressure fields (see Figure 7). To represent the three-dimensional trajectory of blood particles, streamline integration was performed using a fourth-order Runge-Kutta integrator

which allowed the identification of complex fluid structures, such as turbulent vortices and stagnation zones in the aortic arch.

(b) Quantitative data were visualized through longitudinal spatial profiles. Using the `postProcess` utility, scalar pressure and velocity magnitude were sampled along a predefined centerline spline that traversed the entirety of the aorta. This allowed for the generation of linear graphs representing the hemodynamic gradient, where local pressure drops and velocity spikes could be directly correlated with anatomical constrictions and better clinical interpretation as seen in Figure 8, and a much smoother and more progressive pressure decay in the healthy aorta's graph as seen in Figure 9.

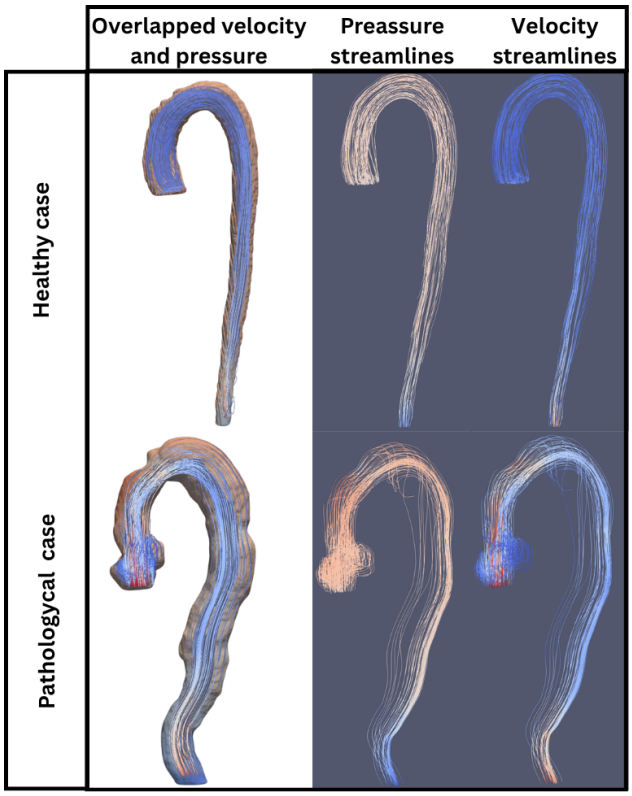



*Figure 7.* Flow patterns for a healthy and pathological aorta, coloring the pressure and velocity streamlines.

## 4. Discussion

The absence of false negatives in the SVM model is a highly desirable characteristic for medical diagnostic software. The success of SVM architectures in this specific application can be attributed to their ability to work on vector spaces, creating discriminative planes in smaller dimensions. This mechanism is well-suited for healthcare, despite a complex

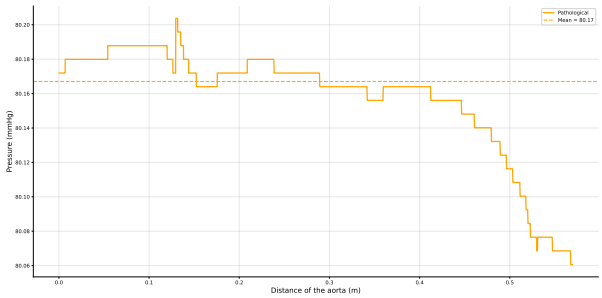



*Figure 8.* Diastolic pressure in a centerline spline across the aorta of a pathological patient.

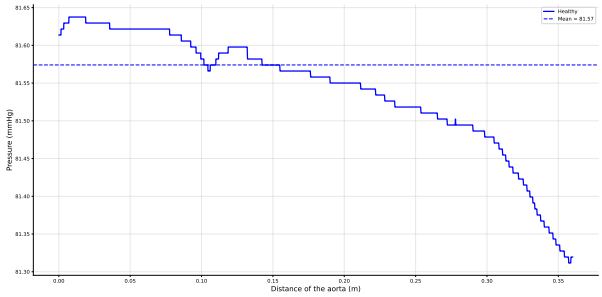



*Figure 9.* Diastolic pressure in a centerline spline across the aorta of a healthy patient.

interpretability (Guido et al., 2024), extending in this case to characterizing aortic conditions, which typically present as inflammation and irregularities within an otherwise uniform aortic tree. It is important to note that the current model does not yet represent a statistically significant sample for AD patients. However, it strongly demonstrates the capability of machine learning to successfully separate outlying pathological cases from a large healthy sample ($n = 76$).

Although the obtained hemodynamic values should not be interpreted as absolute physiological measurements due to the simplified computational domain and the exclusion of supra-aortic and distal branch outlets, the CFD simulations successfully enabled qualitative analysis of aortic flow behavior. Streamline visualization revealed clear differences between the healthy and pathological geometries, where the healthy model exhibited smoother and more organized laminar flow, while the pathological aorta showed disturbed flow patterns, vortex formation, recirculation zones, and localized pressure fluctuations caused by the dissected morphology. Pressure profiles extracted along the centerline spline demonstrated a more irregular pressure distribution in the pathological case, highlighting regions susceptible to altered wall stress and abnormal hemodynamic behavior.

These findings demonstrate the usefulness of CFD-based visualization for identifying biomechanically relevant regions and supporting qualitative interpretation of pathological aortic flow dynamics.

Regarding the final software's estimated performance, it varies with scan size, and hardware limitations. With 2 different workstations, one without a graphics card and one fully equipped workstation, the processing times per study varied from 10 to 3 minutes, without flow simulation, with the biggest time sink being the Total Segmentator, accounting for 1-6 minutes. Flow simulation can be completed in a time lapse of 12 to 16 minutes. Given the requirements for different modules, there is a high parallelization potential, which would reduce time. Hardware specification can be found in supplementary material.

## 5. Limitations

The biggest obstacle to model generalization for a global population is sample size. Despite the multicentric approach, acquired data fell short of the desired amount, by an immense margin. Due to time constraints, individual slice characterization was not performed due to the manual nature of the labeling process, as well as the lack of hands-on medical experts on the team to validate slice choice. Global study characteristics show promise with high importance scores, but augmented data will only allow the distinction to be valid for the original sample size. Total segmentation gives a ROI mask with validated previous results, but it does not segment the intimal flap critical in other AD detection models. This work thus exemplifies a preliminary anomaly detection model, as opposed to a global general diagnostic model.

## 6. Future Work

Directions for future work in model development include, but are not limited to, increasing sample size, transporting model focus from global characteristics only to per-slice characterization with Pyradiomics as well, including a nnU-Net based intimal flap segmentation model, and increasing medical input in the process as a whole. Afterwards, classification tasks can be increased in scope to include other Acute Aortic Syndrome conditions classifiable by ML models, such as Intramural Hematoma and Penetrating Aortic Ulcer.

The next phase training the model to an approach on the identification of clear luminal enhancements and the visible intimal flap from contrast CTs with the subtle hyperdense or structural cues present in non-contrast scans. With the objetive to robusty the identification of the aoritc dissection while precisely localizing the entry tear and mapping the longitudinal extension of the dissection.

In addition, the tool must be packaged to ensure compatibility with various platforms on which it could be deployed as a web application, such as in hospital PACS systems or as a module in imaging systems, in order to optimize the diagnostic process in emergency situations.

## Impact Statement

AD is a critical cardiovascular emergency where rapid diagnosis is directly tied to patient survival. By developing diagnostic support software capable of utilizing NCE-CT, this work expands life-saving diagnostic capabilities to contraindicated patient populations who cannot safely receive contrast agents. Ethically, this not only mitigates the risk of adverse medical events during imaging but also actively shortens the diagnostic window for highly vulnerable individuals. This work represents an initial step into a globalized model that can be integrated into hospitals across the world.

## Acknowledgments

We recognize and thank the collaboration of the following medical specialists: Dr. Mario Alejandro Fabiani, Dr. Mauricio Gonzáles Urquijo, Dr. Mario D'Oria, Dr. Marta Pignataro, Dr. Daniele Morosetti, and Dr. Luis Jimenez Angeles. We also recognize and thank the support of the Computational Robotics Lab, with Dr. Luis Alberto Muñoz Ubando for the shared equipment for sample analysis. For continued guidance, we thank our professors: Dr. Adeodato Israel Botello Arredondo, Dr. Marcos Moya Bencomo, and Dr. Mauricio Adolfo Ramírez Moreno. Finally, we thank MsC Nezih Nieto Gutierrez, for not only supporting and believing in the project, but for course correcting, technique sharing, and trust placed in the team and our abilities. This project was enabled completely by them.

## References

Ahrens, J., Geveci, B., and Law, C. ParaView: An end-user tool for large data visualization. In *Visualization Handbook*. Elsevier, 2005. ISBN 9780123875822.

Armato III, S. G., McLennan, G., Bidaut, L., McNitt-Gray, M. F., Meyer, C. R., Reeves, A. P., Zhao, B., Aberle, D. R., Henschke, C. I., Hoffman, E. A., Kazerooni, E. A., MacMahon, H., Van Beek, E. J. R., Yankelevitz, D., Biancardi, A. M., Bland, P. H., Brown, M. S., Engelmann, R. M., Laderach, G. E., Max, D., Pais, R. C., Qing, D. P. Y., Roberts, R. Y., Smith, A. R., Starkey, A., Batra, P., Caligiuri, P., Farooqi, A., Gladish, G. W., Jude, C. M., Munden, R. F., Petkovska, I., Quint, L. E., Schwartz, L. H., Sundaram, B., Dodd, L. E., Fenimore, C., Gur, D., Petrick, N., Freymann, J., Kirby, J., Hughes, B., Casteele, A. V., Gupte, S., Sallam, M., Heath, M. D., Kuhn,

M. H., Dharaiya, E., Burns, R., Fryd, D. S., Salganicoff, M., Anand, V., Shreter, U., Vastagh, S., Croft, B. Y., and Clarke, L. P. Data from LIDC-IDRI [data set], 2015.

Cardoso, M. J., Li, W., Brown, R., Ma, N., Kerfoot, E., Wang, Y., others, and Feng, A. MONAI: An open-source framework for deep learning in healthcare. *arXiv preprint arXiv:2211.02701*, 2022.

Cheng, Z., Z. L. Y. J. Z. H. L. S. Y. L.-P. C. M. X. X. G. . S. L. A deep learning algorithm for the detection of aortic dissection on non-contrast-enhanced computed tomography via the identification and segmentation of the true and false lumens of the aorta. *Quantitative Imaging in Medicine and Surgery*, 14(10):7365–7378, 2022. doi: 10.21037/qims-24-533.

Dong, F., Song, J., Chen, B., Xie, X., Cheng, J., Song, J., and Huang, Q. Improved detection of aortic dissection in non-contrast-enhanced chest CT using an attention-based deep learning model. *Heliyon*, 10(2):e24547, 2024. doi: 10.1016/j.heliyon.2024.e24547.

Guido, R., Ferrisi, S., Lofaro, D., and Conforti, D. An overview on the advancements of support vector machine models in healthcare applications: a review. *Information*, 15(4):235, 2024. doi: 10.3390/info15040235.

Hu, Y., Xiang, Y., Zhou, Y., He, Y., Lang, D., Yang, S., Du, X., Den, C., Xu, Y., Wang, G., Ding, Z., Huang, J., Zhao, W., Wu, X., Li, D., Zhu, Q., Li, Z., Qiu, C., Wu, Z., others, and Zhang, H. AI-based diagnosis of acute aortic syndrome from noncontrast CT. *Nature Medicine*, 31(11): 3832–3844, 2025. doi: 10.1038/s41591-025-03916-z.

Isensee, F., J. P. F. K. S. A. P. J. . M.-H. K. H. nnu-net: a self-configuring method for deep learning-based biomedical image segmentation. *Information*, 18(2):203–211, 2021. doi: 10.1038/s41592-020-01008-z.

Langley, P. Crafting papers on machine learning. In Langley, P. (ed.), *Proceedings of the 17th International Conference on Machine Learning (ICML 2000)*, pp. 1207–1216, Stanford, CA, 2000. Morgan Kaufmann.

National Lung Screening Trial Research Team. Data from the National Lung Screening Trial (NLST) [data set], 2013.

Rodríguez, F. D. A., Quintero, D. A. A., Moreira, W. D. O., Terán, P. A. G., Pires, L. N. P., Gualpa, E. P. T., Balladares, S. L. L., Cadena, A. M. T., and Aguirre, C. D. L. Diagnosis and treatment of aortic dissection. literature review. *Angiología*, 2023. doi: 10.20960/angiologia.00455.

Sica et al. Imaging features of the false and true lumen in aortic dissection. *Manuscript / source to be confirmed*, 2025. Reference cited in draft; full bibliographic details to be supplied.

Spangenberg, A., Rao, S. J., Mackrell, J., Rimm, S., and Haas, C. J. Type A aortic dissection and non-contrast computed tomography. *Journal of Community Hospital Internal Medicine Perspectives*, 13(3):118–120, 2023. doi: 10.55729/2000-9666.1178.

Umaña, J. P. and Camacho, J. Disección aórtica aguda: diagnóstico y manejo inicial. *Revista Médica Clínica Las Condes*, 33:218–226, 2022. doi: 10.1016/j.rmclc.2022.05.002.

Van Griethuysen, J. J., Fedorov, A., Parmar, C., Hosny, A., Aucoin, N., Narayan, V., Beets-Tan, R. G., Fillion-Robin, J., Pieper, S., and Aerts, H. J. Computational radiomics system to decode the radiographic phenotype. *Cancer Research*, 77(21):e104–e107, 2017. doi: 10.1158/0008-5472.can-17-0339.

Wasserthal, J., Breit, H. C., Meyer, M. T., Pradella, M., Hinck, D., Sauter, A. W., Heye, T., Boll, D. T., Cyriac, J., Yang, S., Bach, M., and Segeroth, M. TotalSegmentator: Robust segmentation of 104 anatomic structures in CT images. *Radiology. Artificial Intelligence*, 5(5):e230024, 2023. doi: 10.1148/ryai.230024.

Weller, H. G., Tabor, G., Jasak, H., and Fureby, C. A tensorial approach to computational continuum mechanics using object-oriented techniques. *Computers in Physics*, 12(6):620–631, 1998.

Zhao, B., Schwartz, L. H., Kris, M. G., and Riely, G. J. Coffee-break lung CT collection with scan images reconstructed at multiple imaging parameters (version 3) [dataset], 2015.

Zhao, Y., Zhang, Y., Zhang, J., Chen, C., Li, P., Li, J., and Fu, Q. Performance of image-based deep learning models for aortic dissection segmentation and diagnosis: a systematic review and meta-analysis. *Frontiers in Cardiovascular Medicine*, 13:1734208, 2026. doi: 10.3389/fcvm.2026.1734208.

Zhou, Z., Yang, J., Wang, S., Li, W., Xie, L., Li, Y., and Zhang, C. The diagnostic value of a non-contrast computed tomography scan-based radiomics model for acute aortic dissection. *Medicine*, 100(22):e26212, 2021. doi: 10.1097/md.0000000000026212.